Stellar (n,γ) cross sections of p-process isotopes
Part 1: ^{102}Pd, ^{120}Te, ^{130,132}Ba, and ^{156}Dy

I. Dillmann*

Physik Department E12 and Excellence Cluster Universe, Technische Universität München, Germany

C. Domingo-Pardo† and M. Heil†

Gesellschaft für Schwerionenforschung Darmstadt, Germany

F. Käppeler and S. Walter

Institut für Kernphysik, Forschungszentrum Karlsruhe, Postfach 3640, D-76021 Karlsruhe, Germany

S. Dababneh

Faculty of Applied Sciences, Al-Balqa Applied University, Salt 19117, Jordan

T. Rauscher and F.-K. Thielemann

Departement Physik, Universität Basel, Klingelbergstrasse 82, CH-4056 Basel, Switzerland

(Dated: March 2, 2013)

We have investigated the (n,γ) cross sections of p-process isotopes with the activation technique. The measurements were carried out at the Karlsruhe Van de Graaff accelerator using the ^{7}Li$(p,n)^7$Be source for simulating a Maxwellian neutron distribution of $kT = 25$ keV. Stellar cross section measurements are reported for the light p-process isotopes ^{102}Pd, ^{120}Te, ^{130,132}Ba, and ^{156}Dy. In a following paper the cross sections of ^{168}Yb, ^{180}W, ^{184}Os, ^{190}Pt, and ^{196}Hg will be discussed. The data are extrapolated to p-process energies by including information from evaluated nuclear data libraries. The results are compared to standard Hauser-Feshbach models frequently used in astrophysics.

PACS numbers: 25.40.Lw, 26.30.-k, 27.50.+e, 97.10.Cv

I. INTRODUCTION

Astrophysical models can explain the origin of most nuclei beyond the iron group by a combination of processes involving neutron captures on long (s-process) or short (r-process) time scales [1, 2].

However, 32 proton-rich stable isotopes between ^{74}Se and ^{196}Hg cannot be formed in these neutron capture processes, because they are either shielded by stable isotopes from the r-process decay chains or lie outside the s-process flow (Fig. 1). These isotopes, which are ascribed to the so-called "p-process", are 10 to 100 times less abundant than their s- and r-process neighbors. So far, the astrophysical site of the p-process is still under discussion, since the solar p-abundances can not be completely described by current models.

Historically, the p-process was thought to proceed via proton captures, but a plausible site with the required amount of free protons could not be identified. Moreover, elements with large Z cannot be produced by proton captures because the temperatures necessary to overcome
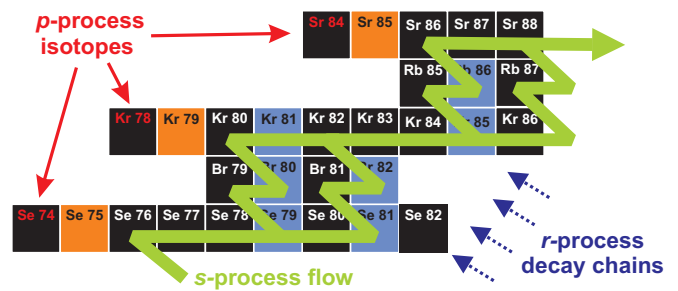
FIG. 1: (Color online) Example from the chart of nuclides illustrating the position of the lightest p-nuclei, which are shielded from the s-process flow and the r-process decay chains.

the Coulomb repulsion favor photodisintegration rather than charged-particle capture.

The most plausible astrophysical site is the explosively burning Ne/O layer in core collapse supernovae, which is heated to ignition temperatures by the outgoing shock front [3–5]. In this high-temperature environment proton-rich nuclei are produced by sequences of photo-dissociations and β^+ decays. In stars 20 times more massive than the sun the p-process temperatures for efficient photo-disintegration are already reached at the end of hydrostatic Ne/O burning [6]. This mechanism is also called "γ process" because proton-rich isotopes are produced by (γ,n) reactions on pre-existing seed nuclei from

the s- and r- processes. When (γ, p) and (γ, α) reactions become comparable or faster than (γ, n), the reaction path branches out from the initial isotopic chain and feeds nuclei with lower atomic number Z. While photodisintegration dominates in the early, hot phase, the initially released neutrons can be recaptured at a later time, when the material cools down after the passage of the shockwave. The typical p-process abundance pattern exhibits maxima at ^{92}Mo (N=50) and ^{144}Sm (N=82).

The solar abundances of the p-nuclei are reproduced by current models of the γ process within factors of two to three on average [5–7], except for two regions with nuclei of $A < 100$ and $150 \leq A \leq 165$ [6]. The most abundant p-isotopes, ^{92,94}Mo and ^{96,98}Ru, are significantly underproduced because appropriately abundant seed nuclei are missing. Alternative processes and sites have been proposed in order to explain this deficiency, i.e. reactions induced by the strong neutrino fluxes in the deepest ejected layers of core-collapse supernovae (the νp process [8]), or explosive hydrogen burning in proton-rich, hot matter accreted onto the surface of neutron stars (the rp process [9, 10]). An alternative site for additional production of the $150 \leq A \leq 165$ has not been suggested so far.

A few p-nuclides may also be produced by neutrino reactions during the γ process. This "ν process" [11] could be the origin of the odd-odd isotopes ^{138}La and ^{180}Ta$^{\rm m}$, which are strongly underproduced in the γ process. The abundances of both p-nuclei may be explained by neutrino scattering on their abundant neighbor isotopes to states above the neutron emission threshold.

The isotopes ^{152}Gd, ^{164}Er, and ^{180}Ta$^{\rm m}$ were sometimes also considered as p-nuclei but it was found that significant fractions are produced indeed by the s-process [12].

The fact that self-consistent studies of the γ process have problems to synthesize the p-nuclei in the mass regions $A < 124$ and $150 \leq A \leq 165$ [6] may result from difficulties related to the astrophysical models as well as from systematic uncertainties of the nuclear physics input. Therefore, the improvement of nuclear reaction cross sections is crucial for further progress in p-process models, either by directly replacing theoretical predictions by experimental data or by testing the reliability of predictions if the relevant energy range is not accessible by experiments.

In this context we have carried out an extensive experimental program to measure the (n, γ) cross sections of 13 p-only isotopes by means of the activation technique. Two publications are already available concerning ^{74}Se, ^{84}Sr [13], and ^{174}Hf [14]. The present paper continues this series of measurements with the isotopes ^{102}Pd, ^{120}Te, ^{130,132}Ba, and ^{156}Dy, and a follow-up paper will cover the remaining heavy p-isotopes ^{168}Yb, ^{180}W, ^{184}Os, ^{190}Pt, and ^{196}Hg. A concluding paper will present p-process network calculations based on a new version of the "Karlsruhe Astrophysical Database of Nucleosynthesis in Stars" (KADoNiS) [15], where the available experimental and semi-empirical (n, γ) cross sections for the p-process will be added to the already existing data library

for the s-process. Thereby, the KADoNiS project will be extended to provide the p-process community with updated experimental information. These data will necessarily remain a complement to the indispensable theoretical predictions for the vast majority of the mostly unstable isotopes in the p-process network, which are not accessible to cross section measurements with present experimental techniques. Nevertheless, these data provide important tests of existing calculations in the Hauser-Feshbach statistical model [16], i.e. with the codes NONSMOKER [17, 18] or MOST [19].

The experimental aspects of this work are presented in Sec. II. The analysis of the data and a discussion of the related uncertainties follows in Secs. III and IV. The results are discussed in Sec. V and the calculated Maxwellian averaged cross sections in Sec. VI.

II. EXPERIMENTAL TECHNIQUE

This section contains a concise discussion of the experimental technique. More detailed information can be found in Refs. [20, 21].

A. Neutron activation

The present capture measurements were carried out at the (now closed) Karlsruhe 3.7 MV Van de Graaff accelerator using the activation technique. Neutrons were produced with the ^{7}Li$(p, n)^{7}$Be source by bombarding 30 μm thick layers of metallic Li or crystalline LiF on water-cooled Cu backings with protons of 1912 keV, 31 keV above the threshold of the ^{7}Li$(p, n)^{7}$Be reaction at 1881 keV. Under these conditions, all neutrons are emitted into a forward cone of 120° opening angle. The resulting neutron field represents a quasi-stellar spectrum, which approximates a Maxwell-Boltzmann distribution for kT= 25.0 $\pm$ 0.5 keV [21] (see Fig. 2). Activation in this spectrum yields, therefore, directly the Maxwellian averaged cross section (MACS), with only a small correction for the fact that the quasi-stellar spectrum is truncated at E_n= 106 keV. Neutron scattering in the Cu backing is negligible, since the transmission is $\approx$98% in the energy range of interest.

In all cases, the sample material was of natural composition and high elemental purity ($\geq$ 99.5%), either in metallic form or as a compound (Table I). However, it has to be emphasized that the large uncertainty of the ^{120}Te abundance given in [22] originates from the fractionation of tellurium in various materials and the fact that up to now no absolute isotopic abundance measurement has been carried out.

The recommended value of 0.09 (1)% in [22] is commented with "An electron multiplier was used for these measurements and the measured abundances were adjusted using a 'square root of the masses' correction factor" [23]. Independent relative measurements of the iso-
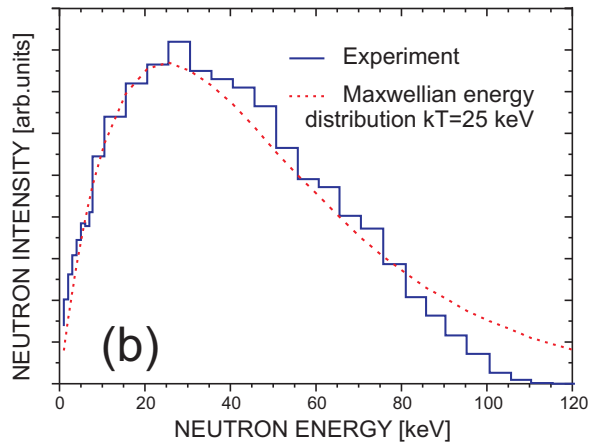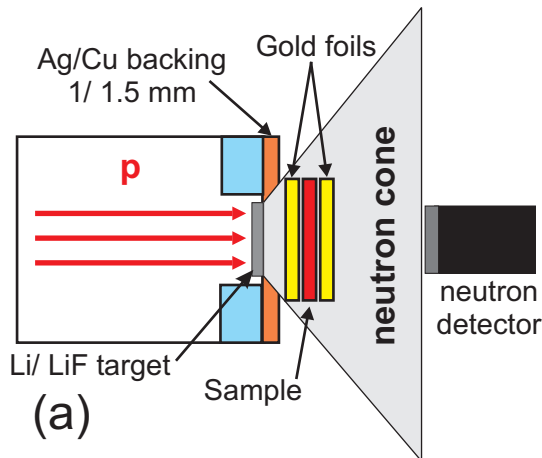
FIG. 2: (Color Online) (a) Schematic sketch of the experimental setup. (b) Comparison of the experimental neutron distribution and a Maxwell distribution of kT=25 keV.

tope ratios have been carried out later by De Laeter et al. [24] with a Faraday Cup collector and Lee et al. [25] using ICP-MS (inductively coupled plasma mass spectrometry). Both methods revealed ^{120}Te abundances of 0.0918 (7)% and 0.0927 (4)%, respectively, which are in clear disagreement with the "best value" assignment of 0.0960 (7)% by Smith et al. [23] given in the latest IU-PAC Technical Report 2003 [22]. In [24] the value from Smith et al. [23] was corrected with the above mentioned factor $\sqrt{m_1/m_2}$ and one can calculate a value of 0.0935 (7)% from the given isotope ratios. The correction is due to a mass discrimination which occurs when using electron multipliers. The signal from light isotopes is enhanced compared to that from heavier isotopes because the secondary electron yield at the first dynode is velocity dependent [24]. The methods using Faraday cups [24] or ICP-MS [25] do already account for this. From these three values we can derive a weighted average of 0.0927 (9)% where the uncertainty is derived from the standard deviation of the measurements. We decided to use this value for our measurement instead of the "representative isotopic composition" given in [22].

TABLE I: Sample materials and isotopic abundances [22]

Element	Isotope	Sample material	Rel. abundance [%]
Pd	^{102}Pd	Pd (metal)	1.02 (1)
Te	^{120}Te	Te (metal)	0.09 (1)[a]
Ba	^{130}Ba	BaCO$_3$	0.106 (1)
	^{132}Ba	BaCO$_3$	0.101 (1)
Dy	^{156}Dy	Dy (metal)	0.056 (3)

[a] See text. Used value is 0.0927 (9)%.

Apart from the Pd samples, which were cut from 25 μm thick foils, thin pellets 6 to 10 mm in diameter were pressed from the respective powder or granules and enclosed in thin cannings made from 15 μm thick aluminum foil. During the irradiations the samples were sandwiched

between 10-30 μm thick gold foils of the same diameter. In this way the neutron flux can be determined relative to the well-known capture cross section of ^{197}Au [21].

The activation measurements were carried out with the Van de Graaff accelerator operated in DC mode with a current of $\approx$100 μA (for the Li targets) or even higher currents (up to 150 μA) for the LiF targets. To ensure homogeneous illumination of the entire surface, the proton beam was continuously wobbled across the Li target. The samples were irradiated in close contact with the Li target with average neutron intensities of (1.5–3)$\times 10^9$ s^{-1} at the position of the samples. The neutron intensity was recorded in intervals of 60 or 90 s using a ^{6}Li-glass detector 91 cm downstream of the lithium target. With this information, fluctuations in the neutron yield could be properly considered in the later correction of the number of nuclei, which decayed during the activation.

Over the course of the present measurements, several independent activations have been carried out for each isotope with modified experimental parameters (see Table II).

B. Activity measurements

For the measurement of the induced activities two detector setups were available. A single high purity Germanium (HPGe) detector with a well defined measuring position at 76.0±0.5 mm from the detector surface was used for counting the activities of the gold foils and of the ^{121}Te, ^{131}Ba, and ^{133}Ba^m decays. The detector was shielded by 10 cm of lead and 5 mm of copper. Energy and efficiency calibrations have been carried out with a set of reference γ-sources in the energy range between 60 keV and 2000 keV (see Fig. 3).

The small γ activities of ^{103}Pd and ^{133}Ba^g were measured with a system of two HPGe Clover detectors (see Ref. [26] for more details). Each Clover detector consists

TABLE II: Sample characteristics and activation parameters.

Target isotope	Sample	Diameter [mm]	Mass [mg]	Mass [10^{18} atoms]	t_a [min]	$\Phi_{tot}{}^a$ [10^{14} n]
^{102}Pd	pd-1	10	452.5	26.1	9770	8.18
	pd-2	8	301.5	17.4	5751	4.83
	pd-3	12	339.5	19.6	7585	3.48
^{120}Te	te-1	10	352.9	1.54	2617	1.96
	te-2	10	441.2	1.93	1600	1.52
	te-3	8	349.3	1.53	1406	1.56
	te-4	8	417.2	1.83	4142	3.03
	te-5	8	409.6	1.79	2593	3.09
^{130}Ba	ba-1	8	106.9	0.346	7721	6.93
^{132}Ba				0.330		
^{130}Ba	ba-2	8	145.5	0.471	4014	2.70
^{132}Ba				0.448		
^{130}Ba	ba-3	10	149.7	0.484	4280	4.48
^{132}Ba				0.461		
^{156}Dy	dy-1	6	28.3	0.0588	964	0.995
	dy-2	10	80.1	0.166	362	0.416
	dy-3	6	61.6	0.128	902	1.73

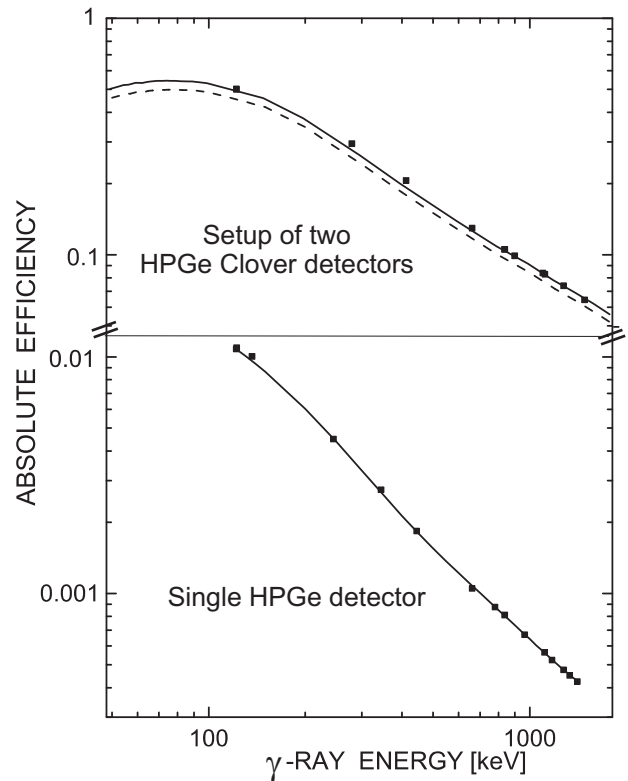[a] Total neutron exposure during activation.

FIG. 3: Efficiency curves of the Clover detector system and the single HPGe detector. The statistical uncertainties of the calibration measurements correspond to the size of the symbols. The simulated efficiency of the Clover system (dashed line) was normalized to fit the measured data points.

of four independent HPGe n-type crystals in a common cryostat. The two Clovers were placed face to face, in contact with a 5.2 mm thick sample holder, corresponding nearly to a 4π geometry. The sample position in the very center of the system could be reproduced within ± 0.1 mm. The whole assembly was shielded against room background with 10 cm of lead and a 5 mm thick layer of copper. The data from the eight Ge crystals of the two Clover detectors were processed by separate analog to digital converters (ADCs) and could, therefore be analyzed independently. In Clover measurements, the contributions of the eight crystals were added to represent the total number of events per γ-ray line. The efficiency calibration of the Clover system was carried out with a set of weak reference sources.

III. DATA ANALYSIS

A. General procedure

The total amount of activated nuclei N_{act} at the end of each irradiation can be deduced from the number of events C in a particular γ-ray line registered in the HPGe detector during the measuring time t_m [20],

$$N_{act} = \frac{C(t_m)}{\varepsilon_\gamma \; I_\gamma \; K \; (1 - e^{-\lambda \; t_m}) \; e^{-\lambda \; t_w}} \qquad (1)$$

where t_w denotes the waiting time between irradiation and activity measurement, ε_γ the efficiency of the HPGe detector, and I_γ the relative γ intensity per decay of the respective transition. K is a correction factor which is either the self-absorption correction factor K_γ (Eq 2) or the total correction factor K_{tot} (Table IV). The decay properties of the investigated product nuclei are summarized in Table III.

The large distance between sample and detector in the measurements with the single HPGe detector allowed us to calculate the correction for γ-ray self-absorption from the expression for disk samples of thickness d [20],

$$K_\gamma = \frac{1 - e^{-\mu d}}{\mu d}, \qquad (2)$$

using the γ-ray absorption coefficients μ from Ref. [33]. This correction factor was negligible for the thin (10-30 μm) gold foils.

The close geometry of the Clover detectors required a more elaborate treatment of the sample-related corrections in the measurement of the small activities of ^{103}Pd and ^{133}Ba^g. The correction factors K'_γ for γ-ray self absorption, K_E for the extended geometry of the sample, and K_S for the summing effect of cascade transitions have the been calculated by means of Monte Carlo simulations with the GEANT4 toolkit [34] and a detailed computer model of the setup [26] (Table IV). The summing correc-

TABLE III: Decay properties of the product nuclei used in the analysis. EC stands for electron capture decay, IT for isomeric transition.

Product nucleus	$t_{1/2}$	Decay mode	E_γ [keV]	I_γ [%]	Reference
^{103}Pd	16.991 (19) d	EC	357.5	0.0221 (7)	[27]
^{121}Te^g	19.16 (5) d	EC	573.1	80.3 (25)	[28]
^{121}Te^m	154 (7) d	IT (88.6 (11) %)	212.2	81.4 (1)	
^{121}Te^m		EC (11.4 (11) %)	1102.1	2.54 (6)	
^{131}Ba	11.50 (6) d	EC	216.1	20.4 (4)	[29]
		EC	496.3	48.0 (4)	
^{133}Ba^g	10.52 (13) yr	EC	356.0	62.05 (19)	[30]
^{133}Ba^m	38.9 (1) h	IT (99.99 %)	275.9	17.8 (6)	
^{157}Dy	8.14 (4) h	EC	326.3	93 (3)	[31]
^{198}Au	2.69517 (21) d	β^-	411.8	95.58 (12)	[32]

tion factor K_S of sample pd-3 is slightly higher than for samples pd-1 and pd-2 due to the varying thickness. The thinner sample pd-3 absorbs less X-rays and thus more coincident summing with decay γ-rays can occur.

TABLE IV: GEANT4 simulations of the correction factors for the ^{103}Pd and ^{133}Ba^g measurements with the Clover detector system.

Sample	Thickness [mm]	K_E	K'_γ	K_S	K_{tot}
pd-1	0.5	0.9976	0.9563	0.9991	0.9531
pd-2	0.5	0.9986	0.9569	0.9951	0.9509
pd-3	0.25	0.9972	0.9762	0.9663	0.9407
ba-1	0.48	1.0002	0.9820	0.9575	0.9405
ba-2	0.65	1.0022	0.9752	0.9608	0.9390
ba-3	0.43	0.9994	0.9841	0.9570	0.9412

The number of activated nuclei N_{act} can be written as

$$N_{act}(i) = \langle\sigma_i\rangle \ N_i \ \Phi_{tot} \ f(i) \quad , \tag{3}$$

where $\Phi_{tot} = \int \phi(t)dt$ is the time-integrated neutron flux and N_i the number of atoms of species i in the sample. As our measurements are carried out relative to ^{197}Au as a standard, the neutron flux Φ_{tot} cancels out in the ratio,

$$\frac{N_{act}(i)}{N_{act}(Au)} = \frac{\langle\sigma_i\rangle \ N_i \ f(i)}{\langle\sigma_{Au}\rangle \ N_{Au} \ f(Au)}$$

$$\Longleftrightarrow \langle\sigma_i\rangle = \langle\sigma_{Au}\rangle \frac{N_{act}(i) \ N_{Au} \ f(Au)}{N_{act}(Au) \ N_i \ f(i)} \quad . \tag{4}$$

The correction factor

$$f = \frac{\int_0^{t_a} \phi(t) \ e^{-\lambda(t_a-t)} \ dt}{\int_0^{t_a} \phi(t) \ dt} \tag{5}$$

for the decay of activated nuclei during the irradiation time t_a is calculated from the neutron flux history recorded with the ^{6}Li glass detector downstream of the neutron target. This correction includes also the effect of variations in the neutron flux.

The cross section $\langle\sigma_{exp}\rangle$ is given in brackets to indicate that it represents an average over the quasi-stellar spectrum of the ^{7}Li(p,n)^{7}Be source. The reference value for the experimental averaged ^{197}Au cross section was adopted as $\langle\sigma_{exp}\rangle$=586 ± 8 mbarn [21].

B. Partial cross sections

In the activations of ^{120}Te, ^{130}Ba, and ^{132}Ba, neutron capture populates ground and isomeric states in the product nucleus. The partial cross section to ^{131}Ba^m could not be measured in this work because the isomer is too short short-lived ($t_{1/2} = 14.6$ min). Therefore, only the total capture cross section of ^{130}Ba was derived from the ground state activity after an appropriate waiting time. Similarly, the isomeric state in ^{133}Ba decays with 99.99% probability by internal transitions with a half-life of 38.9 h so that the total cross section can later be derived from the ground-state activity ($t_{1/2} = 10.52$ yr). In this case, the isomer lived long enough that the partial cross section could be determined as well.

In cases where the half-lives of ground state and isomer are of the same order of magnitude, as for ^{121}Te, where

the isomer (88.6% IT, 11.4% EC) is even longer-lived than the ground-state, the contributions of both states to the total cross section have to be properly disentangled. The partial cross section to the ground state can be deduced from the γ spectra of the first few days, where the contribution from the isomer decay is still small. The exact correction for the ground-state was discussed in detail in Ref. [13] and has been used here.

IV. UNCERTAINTIES

The experimental uncertainties are summarized in Table V. Since nearly every stellar neutron cross section measurement was carried out relative to gold, the 1.4% uncertainty of the gold cross section [21] cancels out in most astrophysical applications.

Significant uncertainties were contributed by the sample position, detector efficiencies, and γ-ray intensities. In the activations the position of the samples relative to the Au foils was estimated to ± 0.25 mm, leading to a 2% uncertainty in the neutron flux. The same uncertainty had to be assigned to the efficiency calibration of both detector systems. The largest uncertainties were in most cases introduced by the adopted γ-ray intensities, I_γ, an aspect that can be improved if more accurate spectroscopic data become available.

Minor uncertainties arise from the sample masses, which were determined to ± 0.1 mg, self absorption corrections, and counting statistics. The isotopic compositions also exhibit rather small uncertainties, except for ^{120}Te and ^{156}Dy, where 11.1% and 5.4% are assigned in Ref. [22], respectively (Table I). Similar to other rare isotopes, i.e. ^{184}Os, ^{190}Pt, or ^{180}Ta, the uncertainties were conservatively treated to "cover the range of probable isotope-abundance variations among different materials as well as experimental errors" [22]. As described in Sec. II we have therefore for ^{120}Te calculated a weighted average of two recent measurements [24, 25] and a corrected value from an older measurement [23, 24] with a standard deviation of 0.9%.

Summing corrections are another potential source of uncertainties. In the measurements with the single HPGe detector these corrections are small due to the low efficiency and can be completely avoided by selecting cascades with only one strong transition. In case of the measurements with the Clover system, the summing corrections were determined by detailed GEANT simulations [34] of the complete setup [26]. Since these corrections turned out to be rather small (Table IV) the related uncertainties have almost no impact on the final results.

In all cases, the total uncertainties include the 2.0-2.2% uncertainty of the gold measurements.

V. RESULTS

In this section, the results of the present work are presented in tabular form with a short discussion of the various measurements. The comparison with previous results will be given in the Sec. VI for the Maxwellian average cross sections $\langle\sigma\rangle_{kT}$ calculated on the basis of the measured $\langle\sigma_{exp}\rangle$ reported here.

A. ^{102}Pd(n,γ)^{103}Pd

Due to the weak γ transitions the activated samples were counted with the Clover system. The γ spectra of the Pd samples were analyzed via the "strongest" transition in ^{103}Rh at 357 keV. The second strongest transition at 497 keV was already too weak and could not be analyzed. The experimental neutron capture cross section is $\langle\sigma_{exp}\rangle = 376 \pm 17$ mbarn (Table VI).

B. ^{120}Te(n,γ)^{121}Te

The Te samples were analyzed via the 573 keV γ-line from the β^+ decay of ^{121}Te^g into ^{121}Sb. The partial cross section to the isomeric state could be determined only after a waiting time of 80 d, when the large Compton background around 210 keV, which was observed immediately after the irradiation, was sufficiently reduced to reveal the expected 212 keV line from the IT decay to the ground state. The results are 470.6$\pm$22.7 mbarn for the neutron capture cross section to the ground-state and 67.6$\pm$2.9 mbarn for the partial cross section to the isomeric state, leading to a total (n,γ) cross section of $\langle\sigma_{exp}\rangle = 538.2\pm25.6$ mbarn (Table VII).

C. ^{130}Ba(n,γ)^{131}Ba

The ^{130}Ba cross section has been measured via the transitions at 216 and 373 keV from the β^+ decay into ^{131}Cs. The two strongest transitions, 124 keV (I_γ=29.8 (3) %) and 496 keV (I_γ=48.0 (4) %), were not used in this analysis because these lines are affected by coincidence summing effects (summing-out into the 620 keV transition). Due to the short isomeric half-life of 14.6 min the partial cross section to the isomer could not be determined. The resulting total experimental cross section is $\langle\sigma_{exp}\rangle = 736\pm29$ mbarn (Table VIII).

D. ^{132}Ba(n,γ)^{133}Ba

For ^{132}Ba the partial cross section to the isomeric state ($t_{1/2} = 38.9$ h) could be measured in addition to the total (n,γ) cross section. The latter measurement was performed with the Clover detector because of the long

TABLE V: Compilation of uncertainties.

Source of uncertainty	Uncertainty (%)							
	^{197}Au	^{102}Pd	^{120}Te→g	^{120}Te→m	^{130}Ba [a]	^{132}Ba→m	^{132}Ba→g+m	^{156}Dy
Gold cross section	1.4[b]	–	–	–	–	–	–	–
Isotopic abundance	–	1.0	0.9	0.9	0.9	1.0	1.0	5.4
Detector efficiency	2.0				2.0			
Divergence of flux	–				2.0			
Sample mass	0.2	–	–	–	–	–	–	0.1
γ-Ray intensity	0.1	3.1	3.1	0.1	1.5/1.4	3.4	0.3	3.2
γ-Ray self-absorption	–				0.2			
Summing corrections	–	0.4	–	–	–	–	0.4	–
Counting statistics	0.1 - 1.0	0.3 - 0.6	0.4 - 0.8	2.0-2.6	0.4 - 1.4	2.6 - 3.1	1.2 - 1.4	1.2 - 2.4
Total uncertainty[c]		4.8	4.8	4.1 - 4.5	3.7 - 4.0	5.4 - 5.8	3.6 - 3.9	7.3 - 7.6

[a] γ-Ray lines at 216 and 373 keV.
[b] Not included in final uncertainty, see text.
[c] Including the respective uncertainty of gold (2.0-2.2%).

TABLE VI: Measured (n,γ) cross sections of ^{102}Pd and total uncertainties.

Sample	$\langle\sigma_{exp}\rangle$ [mbarn]
	E_γ= 357 keV
pd-1	374 ± 18
pd-2	357 ± 17
pd-3	403 ± 19
Weighted average	376 ± 17

TABLE VIII: Measured (n,γ) cross sections of ^{130}Ba and total uncertainties.

Sample	$\langle\sigma_{exp}\rangle$ [mbarn]	
	E_γ= 216 keV	373 keV
ba-1	724 ± 29	737 ± 29
ba-2	748 ± 29	752 ± 30
ba-3	718 ± 27	743 ± 29
Weighted average	736 ± 29	

TABLE VII: Measured (n,γ) cross sections of ^{120}Te and total uncertainties.

Sample	$\langle\sigma_{exp}\rangle$ [mbarn]	
	→^{121}Te^g	→^{121}Te^m
	E_γ= 573 keV	212 keV
te-1	474.4±22.9	66.6±2.8
te-2	465.5±22.4	70.1±2.9
te-3	484.0±23.2	66.5±2.8
te-4	462.2±22.3	65.7±2.9
te-5	468.2±22.7	69.4±3.1
Weighted average	470.6±22.7	67.6±2.9
Total (n,γ) cross section	538.2±25.6	

TABLE IX: Measured (n,γ) cross sections of ^{132}Ba and total uncertainties.

Sample	$\langle\sigma_{exp}\rangle$ [mbarn]	
	→^{133}Ba^{tot}	→^{133}Ba^m
	E_γ= 356 keV	276 keV
ba-1	396.0±15.2	32.7±1.9
ba-2	403.9±15.6	39.6±2.3
ba-3	381.8±13.7	35.4±1.9
Weighted average	392.8±14.8	35.5±2.0

half life of ^{133}Ba^g ($t_{1/2} = 10.52$ yr). The partial cross section to the isomer ^{133}Ba^m was measured via the 276 keV line (99.99% IT) to $\langle\sigma_{exp}\rangle^m = 35.5 \pm 2.0$ mbarn. The EC part of the isomeric decay is only 0.0096% and was, therefore, neglected. The total capture cross section of $\langle\sigma_{exp}\rangle = 393 \pm 15$ mbarn was determined via the strongest transition in the EC decay to ^{133}Cs at 356.0 keV (Table IX).

E. ^{156}Dy(n,γ)^{157}Dy

The (n,γ) cross section of ^{156}Dy was measured via the strongest line in the decay of ^{157}Dy at 326 keV. The uncertainty of the measured value $\langle\sigma_{exp}\rangle = 1641 \pm 117$ mbarn (Table X) is dominated by the contributions from the γ-ray intensity (3.2%) and from the isotopic abundance (5.4%).

TABLE X: Measured (n,γ) cross sections of ^{156}Dy and total uncertainties.

Sample	$\langle\sigma_{exp}\rangle$ [mbarn] E_γ= 326 keV
dy-1	1669 ± 121
dy-2	1638 ± 114
dy-3	1619 ± 114
Weighted average	1641 ± 117

F. Isomeric ratios

Isomeric ratios

$$R_{\rm iso} = \frac{\langle\sigma_{exp}\rangle^{\rm m}}{\langle\sigma_{exp}\rangle^{\rm tot}} \qquad (6)$$

were calculated for ^{121}Te and ^{133}Ba from the measured partial and total (n,γ) cross sections. The present results at kT=25 keV are 0.126±0.012 and 0.090±0.009, respectively. These results are compatible with the thermal values at kT= 25 meV, which are 0.145±0.026 for ^{121}Te and 0.071 for ^{133}Ba [35, 36].

VI. MAXWELLIAN AVERAGED CROSS SECTIONS

A. General remarks

In an astrophysical environment with temperature T, interacting particles are quickly thermalized by collisions in the stellar plasma, and the neutron energy distribution can be described by a Maxwell-Boltzmann spectrum:

$$\Phi = dN/dE_n \sim \sqrt{E_n} \cdot {\rm e}^{-E_n/kT}. \qquad (7)$$

The experimental neutron spectrum of the ^{7}Li$(p,n)^7$Be reaction simulates the energy dependence of the flux $v \cdot \Phi \sim E_n \cdot e^{-E_n/kT}$ with kT=25.0 ± 0.5 keV almost perfectly [21]. However, the cutoff at E_n= 106 keV and small deviations from the shape of the ideal Maxwellian spectrum require a correction of the measured cross section $\langle\sigma_{exp}\rangle$ for obtaining a true Maxwellian average, $\langle\sigma\rangle_{25\ keV}$. This correction is determined by means of the energy-dependent cross sections from data libraries.

B. Evaluated cross sections from data libraries

The corrections for the spectrum differences as well as the extrapolations of the MACS to lower and higher values of kT were determined with the evaluated energy-dependent cross sections, $\sigma(\mathrm{E}_n)$, from the data libraries provided by the online database JANIS 3.0 ("Java-based Nuclear Information Software", www.nea.fr/janis/) [37].

The libraries used were the "Joint Evaluated Fission and Fusion General Purpose File" (JEFF 3.0A and JEFF 3.1, www.nea.fr/html/dbdata/JEFF/), the "Japanese Evaluated Nuclear Data Library" (JENDL 3.3 [38], wwwndc.tokai-sc.jaea.go.jp/jendl/), and the "Evaluated Nuclear Data File" (ENDF-B/VII.0 [39], www.nndc.bnl.gov/), which are partially based on experimental resonance parameters.

TABLE XI: Upper limits (in eV) of the resolved resonance region in different databases. Cases without resonance information are indicated by empty entries.

Isotope	JEFF 3.0A	JEFF 3.1	JENDL 3.3	ENDF-B/VII.0
^{102}Pd	397	397	250	820
^{120}Te	–	–	–	–
^{130}Ba	2030	2530	2530	2800
^{132}Ba	–	–	–	130
^{156}Dy	101.3	–	–	91

For the investigated cases, the most recent data for $\sigma(\mathrm{E}_n)$ are provided by ENDF-B/VII.0, which makes use of resonance parameters from the latest evaluation [36]. The differences between the four data libraries with respect to the resolved resonance region (RRR) are summarized in Table XI. Table XII shows that the contributions of the RRR to the respective Maxwellian averaged cross sections for kT=5-100 keV are almost negligible, except for the lower temperatures in ^{130}Ba, where the RRR reaches up to about 3 keV. In all libraries, the (n,γ) cross sections in the unresolved resonance region (URR) were obtained by Hauser-Feshbach (HF) calculations. Since this region contributes the most important part to the extrapolation towards the higher temperatures of the p-process, it is discussed in more detail.

The Hauser-Feshbach calculations in the JENDL-3.3 evaluations were performed with the statistical model code CASTHY [40] for the isotopes investigated in this work. More specifically, the γ-ray strength function for ^{132}Ba was adjusted to reproduce the available experimental capture cross section of Ref. [41]. For JEFF-3.0A, the HF calculations are not documented, and in JEFF-3.1 an unspecified HF prediction with a Moldauer potential was used for ^{102}Pd and ^{120}Te, whereas the CASTHY code was also used for the URR of ^{130,132}Ba. In ENDF/B-VII.0, the URR in ^{102}Pd was obtained with the GNASH code [42], and for ^{156}Dy results from EMPIRE [43] were used. For ^{120}Te and ^{130,132}Ba the respective URR cross sections from JENDL-3.3 have been adopted also in ENDF/B-VII.0.

C. Calculation of Maxwellian average cross sections

In a first step, the evaluated cross sections were folded with the experimental neutron spectrum. The ratios of the measured cross sections and the corresponding aver-

TABLE XII: Contribution of the resolved resonance region to the Maxwellian averaged cross sections (in %) for kT=5-100 keV.

kT [keV]	5	10	15	20	25	30	40	50	60	80	100
						^{102}Pd					
JEFF 3.0A	2.5	0.9	0.5	0.3	0.3	0.2	0.1	0.1	0.1	0	0
JEFF 3.1	2.5	0.9	0.5	0.3	0.3	0.2	0.1	0.1	0.1	0	0
JENDL 3.3	1.4	0.5	0.3	0.2	0.1	0.1	0.1	0	0	0	0
ENDF-B/VII.0	4.4	1.8	1.0	0.7	0.5	0.4	0.3	0.2	0.1	0.1	0.1
						^{130}Ba					
JEFF 3.0A	8.1	3.8	2.4	1.6	1.2	1.0	0.6	0.5	0.4	0.2	0.2
JEFF 3.1	12.5	5.7	3.2	2.0	1.5	1.2	0.9	0.7	0.5	0.3	0.2
JENDL 3.3	12.5	5.7	3.2	2.0	1.5	1.2	0.9	0.7	0.5	0.3	0.2
ENDF-B/VII.0	11.6	5.2	3.1	2.1	1.5	1.1	0.7	0.5	0.4	0.2	0.2
						^{132}Ba					
ENDF-B/VII.0	1.5	0.5	0.3	0.2	0.1	0.1	0.1	0	0	0	0
						^{156}Dy					
JEFF 3.0A	0.7	0.3	0.2	0.1	0.1	0.1	0	0	0	0	0
ENDF-B/VII.0	0.5	0.2	0.1	0.1	0.1	0	0	0	0	0	0

TABLE XIII: Normalization factors $F_{\mathrm{norm}} = \langle\sigma_{\mathrm{exp}}\rangle/\langle\sigma_{\mathrm{eval}}\rangle$ for adjusting the evaluated cross sections in the URR. The factors $\langle\sigma_{\mathrm{exp}}\rangle/\langle\sigma_{\mathrm{HF}}\rangle$ for the pure Hauser-Feshbach models MOST [19] and NON-SMOKER [17, 44] are also listed.

	^{102}Pd	^{120}Te	^{130}Ba	^{132}Ba	^{156}Dy
JEFF 3.0A	1.852	–	0.990	0.870	1.069
JEFF 3.1	1.852	1.263	1.024	0.869	–
JENDL 3.3	0.967	1.843	1.025	0.873	–
ENDF-B/VII.0	0.818	1.843	1.028	0.873	1.059
NON-SMOKER	0.985	0.978	1.019	0.840	1.518
MOST 2005[a]	0.550	1.752	1.505	1.746	0.781

[a]Including stellar enhancement factors without further specification.

ages of the evaluated data,

$$F_{\mathrm{norm}} = \frac{\langle\sigma_{\mathrm{exp}}\rangle}{\langle\sigma_{\mathrm{eval}}\rangle} \quad , \tag{8}$$

are listed in Table XIII for all investigated cases. Since the RRR contributes an almost negligible part to the MACS at higher temperatures, F_{norm} can be used in very good approximation as normalization factor for the URR. This holds even for ^{130}Ba, where the RRR contributes sensibly at lower thermal energies, because in this case the F_{norm} values are very close to unity.

In principle, a full normalization of the evaluated data would change the thermal cross section as well as the resolved resonances. Since these data are (partially) based on experimental information, the contribution from the RRR has been decoupled from the normalization procedure and the MACS were calculated using the RRR con-

tributions listed in Table XII. The contribution from the URR was then determined from the renormalized part of the evaluated cross sections, which consist of theoretical data obtained in HF calculations:

$$\langle\sigma\rangle_{kT} = \langle\sigma\rangle_{kT}^{\mathrm{RRR}} + F_{\mathrm{norm}} \cdot \langle\sigma\rangle_{kT}^{\mathrm{URR}}. \tag{9}$$

This expression is equivalent to obtaining a Maxwellian average from the energy-differential cross section $\sigma(E_{\mathrm{n}})$ after only the URR has been modified (Eq. 10). The respective Maxwellian averaged cross sections are

$$\langle\sigma\rangle_{kT} = \frac{2}{\sqrt{\pi}} \left[\frac{\int^{\mathrm{RRR}} \sigma(E_{\mathrm{n}}) \cdot E_{\mathrm{n}} \cdot e^{-E_{\mathrm{n}}/(kT)} \, dE_{\mathrm{n}}}{\int^{\mathrm{RRR+URR}} E_{\mathrm{n}} \cdot e^{-E_{\mathrm{n}}/(kT)} \, dE_{\mathrm{n}}} + \frac{\int^{\mathrm{URR}} F_{\mathrm{norm}} \cdot \sigma(E_{\mathrm{n}}) \cdot E_{\mathrm{n}} \cdot e^{-E_{\mathrm{n}}/(kT)} \, dE_{\mathrm{n}}}{\int^{\mathrm{RRR+URR}} E_{\mathrm{n}} \cdot e^{-E_{\mathrm{n}}/(kT)} \, dE_{\mathrm{n}}} \right] . \tag{10}$$

The values for thermal energies between kT=5 and 100 keV in Table XIV were derived by normalization with the respective factors F_{norm} listed in Table XIII. Evaluations yielding the same normalization factors are (obviously) based on the same resonance parameters (see discussion in Sec. VI B). Additionally the original and normalized values from the recommendations in Bao et al. [45] are listed in Table XIV for comparison. Note that the previous semi-empirical estimates for ^{102}Pd, ^{120}Te, and ^{132}Ba in the Bao et al. compilation [45] were based on scaled NON-SMOKER predictions (see Sec. VI D for further details).

As can be seen in Table XIV extrapolation to lower or higher energies reveal large differences. For this reason we cannot recommend one or the other evaluation in this paper and leave it to the reader which energy dependence to use.

TABLE XIV: Maxwellian averaged cross sections $\langle\sigma\rangle_{kT}$ (in mbarn) and stellar enhancement factors (f*) for kT=5-100 keV. Listed are the normalized Maxwellian averaged cross sections from the evaluations, and the original and normalized values from Ref. [45].

kT [keV]	5	10	15	20	25	30	40	50	60	80	100
						^{102}Pd						
Bao [45]	894	657	540	466	414	375±118[a]	320	283	257	222	199
Bao norm.	875	643	529	456	405	367±17	313	277	252	217	195
ENDF/B-VII.0	835±41	611±29	511±24	449±21	405±18	371±17	323±15	292±13	270±12	243±11	225±10
JEFF-3.0A/3.1	913±41	657±30	534±24	458±21	404±18	365±16	311±14	275±12	250±11	218±10	198±9
JENDL-3.3	905±36	644±27	527±23	455±20	406±18	370±17	321±15	289±13	267±12	239±11	222±10
f* [17]	1.000	1.000	1.000	1.000	1.000	1.000	1.000	1.000	1.000	1.003	1.011
						^{120}Te						
Bao [45]	1037	708	578	504	455	420±103[a]	372	341	318	286	263
Bao norm.	1331	909	742	647	584	539±26	477	438	408	367	337
ENDF/B-VII.0	1319±58	919±42	749±35	649±31	583±28	535±26	472±22	431±21	403±19	368±18	348±17
JEFF-3.1	1215±63	880±44	733±36	645±31	585±28	540±26	478±22	436±21	407±19	368±18	345±17
JENDL-3.3	1319±58	919±42	749±35	649±31	583±28	535±26	472±22	431±21	403±19	368±18	348±17
f* [17]	1.000	1.000	1.000	1.000	1.000	1.000	1.000	1.000	1.000	1.003	1.010
						^{130}Ba						
Bao [45]	2379	1284	1031	901	818	760±110	683	634	601	556	526
Bao norm.	2333	1259	1011	884	802	745±29	670	622	589	545	516
ENDF/B-VII.0	1600±67	1163±45	979±38	874±34	805±31	756±29	687±27	642±25	610±24	568±22	542±21
JEFF-3.0/A	1862±64	1291±45	1040±38	894±34	797±31	728±29	635±27	575±25	532±24	470±22	425±21
JEFF-3.1	1634±69	1171±45	982±38	874±34	804±31	754±29	686±27	640±25	608±24	566±22	540±21
JENDL-3.3	1634±69	1171±45	982±38	874±34	804±31	754±29	686±27	640±25	608±24	566±22	540±21
f* [17]	1.000	1.000	1.000	1.000	1.000	1.000	1.000	1.002	1.006	1.024	1.056
						^{132}Ba						
Bao [45]	1029	659	526	455	410	379±137[a]	339	315	298	276	261
Bao norm.	1070	685	547	473	426	394±15	353	328	310	287	271
ENDF/B-VII.0	929±35	641±24	530±20	468±18	427±16	398±15	358±14	331±13	313±12	290±11	277±11
JEFF-3.0A/3.1	915±35	637±24	528±20	467±18	426±16	397±15	357±14	331±13	312±12	290±11	276±11
JENDL-3.3	915±35	637±24	528±20	467±18	426±16	397±15	357±14	331±13	312±12	290±11	276±11
f* [17]	1.000	1.000	1.000	1.000	1.000	1.000	1.000	1.001	1.004	1.018	1.040
						^{156}Dy						
Bao [45]	5442	2712	2126	1850	1682	1567±145	1412	1307	1229	1117	1039
Bao norm.	5742	2862	2243	1952	1775	1653±118	1490	1379	1297	1179	1096
ENDF/B-VII.0	4742±336	3012±214	2355±168	2001±143	1775±126	1616±115	1408±100	1274±91	1180±84	1052±75	968±69
JEFF-3.0A	4060±288	2710±193	2216±158	1948±139	1775±126	1651±118	1478±105	1359±97	1269±91	1142±81	1056±75
f* [17]	1.000	1.000	1.001	1.007	1.022	1.046	1.106	1.163	1.210	1.283	1.341

[a] Semi-empirical estimates.

The uncertainties given for the evaluations were derived from Eq. 9. For the contribution of the RRR we assumed a conservative uncertainty of 20%. The uncertainty of each data point in the evaluation is not provided, so $\Delta\langle\sigma_{eval}\rangle$ must be set to 0 and ΔF_{norm} is defined as $\frac{\Delta\langle\sigma_{exp}\rangle}{\langle\sigma_{eval}\rangle}$. $\Delta\langle\sigma\rangle_{kT}^{\mathrm{URR}}$ is the uncertainty of the URR which is based on Hauser-Feshbach predictions. The es-

timate for this uncertainty is even more difficult, but could be done in principle by comparing different Hauser-Feshbach models which use different input parameters, as in our cases (see discussion in Sec. VI B). The large deviations among the different evaluations towards higher energies reflect the influence of the input parameters, but for the individual evaluations we set $\Delta\langle\sigma\rangle_{kT}^{\mathrm{URR}}$=0. Thus

the quoted total uncertainty $\Delta\langle\sigma\rangle_{kT}$ is

$$\Delta\langle\sigma\rangle_{kT} = \sqrt{\left(\Delta\langle\sigma\rangle_{kT}^{\mathrm{RRR}}\right)^2 + \left(\Delta F_{norm}\cdot\langle\sigma\rangle_{kT}^{\mathrm{URR}}\right)^2}. \quad (11)$$

In view of the remaining uncertainties, in particular at higher neutron energies, time-of-flight (TOF) data with experimental uncertainties are needed to replace the present extrapolations.

Since experimentally determined cross sections refer only to target nuclei in their ground states, the effective stellar cross sections have to be corrected for the fact that low-lying excited nuclear states can be thermally populated in the hot stellar photon bath. This is achieved by introducing the stellar enhancement factor (Eq. 12)

$$f^*(T) = \frac{\langle\sigma\rangle^*}{\langle\sigma\rangle^{\mathrm{lab}}} = \frac{\sigma^*}{\sigma^{\mathrm{lab}}} \quad , \quad\quad (12)$$

where the stellar cross section

$$\sigma^* = \frac{\sum_\mu (2J_\mu+1)e^{-E_\mu/(kT)}\sum_\nu \sigma^{\mu\nu}}{\sum_\mu(2J_\mu+1)e^{-E_\mu/(kT)}} \quad\quad (13)$$

accounts for the transitions of thermally populated target states μ to all possible final states ν, whereas the laboratory cross section $\sigma^{\mathrm{lab}} = \sum_\nu \sigma^{0\nu}$ only includes the ground state of the target nuclei. The stellar enhancement factors are tabulated, e.g., in Refs. [17, 44, 45], and can increase strongly with temperature. While the values remain close to unity under typical s-process conditions, they become significantly larger at the higher temperatures of the p-process (Table XVI).

D. Comparison of 30 keV MACS with previous data

The comparison with previous recommendations [45, 46], experimental data [41, 47], and theoretical predictions [17, 19, 48–50] is summarized in Table XV for the MACS at $kT = 30$ keV.

The cross sections of ^{102}Pd, ^{120}Te, and ^{132}Ba had not been measured in the stellar energy range so far. Therefore, the recommended cross sections in the compilation of Bao *et al.* [45] are semi-empirical estimates, using NON-SMOKER results [17] normalized to the local cross section systematics of neighboring nuclei.

The only previous experimental value for ^{130}Ba in the keV region was measured with a filtered neutron beam of 24 ± 2 keV [41]. The result of 715 ± 58 mbarn was transformed into a MACS at $kT = 30$ keV of 761 mbarn [45], in good agreement with the more accurate value of this work.

Also for ^{156}Dy a previous measurement has been reported [47] that was performed with the same activation technique used here, but only a single activation had been made and the result was given as a preliminary value. Nevertheless, there is fair agreement with the result obtained in the present series of activations.

The measurements cover a considerable mass range and consider nuclei with different properties which makes a comparison to predictions interesting but difficult to interpret. The NON-SMOKER predictions for ^{102}Pd, ^{120}Te, ^{130}Ba, and – to some extent – for ^{132}Ba have been confirmed by the experimental results, but the prediction for ^{156}Dy is too low by 28%, similar to the situation for ^{160}Dy. These isotopes are strongly deformed but so are the heavier, stable Dy isotopes. Since the level density of the proton-rich isotopes is high one might expect that the Hauser-Feshbach model would be more reliable. Accordingly, the HF parameterization has to be checked in these cases. The contribution of single resonances, implicitly included in the measurement of the MACS, may be stronger than predicted by the Hauser-Feshbach approach.

The predictions from MOST had to be derived from the stellar reaction rates given in Ref. [19], which already include unspecified stellar enhancement factors (see Eq. 12). These factors should be close to unity for $kT=30$ keV. The values from MOST [19] show significant deviations from the measured data for all considered nuclei, ranging from as much as -45% for ^{102}Pd to +75% for ^{132}Ba at $kT = 30$ keV.

E. Extrapolation to p-process energies

Maxwellian averaged cross sections are also needed at the higher temperatures of the p-process of $2-3$ GK, corresponding to thermal energies of $kT = 170 - 260$ keV. Using the energy-dependencies of the normalized evaluated cross sections discussed before, this extrapolation yields the MACS listed in Table XVI. In this energy range any contributions from the RRR are completely negligible but the uncertainties introduced by the extrapolation become significant.

The stellar reaction rate can be determined via

$$N_A \cdot \langle\sigma v\rangle = 26445.5 \cdot f^* \cdot \langle\sigma\rangle_{kT} \cdot \sqrt{kT/\mu} \quad , \quad (14)$$

with μ being the reduced mass, f^* the stellar enhancement factor (Eq. 12), and N_A the Avogadro constant. With the given numerical prefactor, the units for the MACS, $\langle\sigma\rangle_{kT}$, the thermal energy kT, and the reaction rate $N_A\langle\sigma v\rangle$ are [mbarn], [keV], and [cm^3 mole^{-1} s^{-1}], respectively.

A comparison between the normalized values from this work and the predictions of NON-SMOKER [17, 44] and MOST [19] is shown in Fig. 4. As can be seen and was already mentioned before, the individual evaluated data sets increasingly deviate the further the energy is from the normalization point at kT=25 keV (T=0.29 GK).

Although the MOST results include the stellar enhancement factors, it is only a small correction at 25 keV as can be seen in Table XIV. It has to be emphasized again that the comparison for energies $E_{\mathrm{n}} > 25$ keV is actually a comparison with weighted Hauser-Feshbach pre-

TABLE XV: Comparison of Maxwellian averaged cross sections (in mbarn) at kT=30 keV.

Reference	^{102}Pd	^{120}Te	^{130}Ba	^{132}Ba	^{156}Dy
Bao norm.	367±17	539±26	745±29	394±15	1653±118
ENDF/B-VII.0	371±17	535±26	756±29	398±15	1616±115
JEFF-3.0A	365±16	–	728±29	397±15	1651±118
JEFF-3.1	365±16	540±26	754±29	397±15	–
JENDL-3.3	370±17	535±26	754±29	397±15	–
Experimental data					
Bradley *et al.* [41]	–	–	761±62	–	–
Beer [47]	–	–	–	–	1589±145
Recommended data in compilations					
Bao *et al.* [45]	375±118[a]	420±103[a]	760±110	379±137[a]	1567±145
Allen [46]	320	400	2000	650	870
Theoretical predictions					
Holmes *et al.* [48]	247	275	397	250	1840
Harris [49]	363	776	1012	442	1637
Zhao *et al.* [50]	137±45	293±96	–	280±92	850±280
NON-SMOKER [17]	323	506	605	374	1190
MOST [19][b]	665	307	490	227	2126

[a] Semi-empirical estimates.
[b] Includes unspecified stellar enhancement factors.

TABLE XVI: Maxwellian averaged cross sections $\langle\sigma\rangle_{kT}$ (in mbarn) and stellar enhancement factors (f*) [17, 44] at p-process temperatures.

kT [keV]	170	215	260
^{102}Pd			
ENDF/B-VII.0	191±9	177±8	168±8
JEFF-3.0A/3.1	164±7	151±7	141±6
JENDL-3.3	192±9	182±8	173±8
f* [17]	1.11	1.19	1.27
^{120}Te			
ENDF/B-VII.0 / JENDL-3.3	311±15	296±14	284±14
JEFF-3.1	304±15	291±14	281±14
f* [17]	1.10	1.18	1.25
^{130}Ba			
ENDF/B-VII.0	505±20	500±20	503±20
JEFF-3.0A	323±20	280±20	248±20
JEFF-3.1/JENDL-3.3	504±20	499±20	501±20
f* [17]	1.23	1.35	1.42
^{132}Ba			
Evaluations	258±10	254±10	253±10
f* [17]	1.16	1.23	1.28
^{156}Dy			
ENDF/B-VII.0	819±58	772±55	738±53
JEFF-3.0A	895±64	841±60	802±57
f* [17]	1.50	1.55	1.56

dictions which are implicitly contained in the databases (see the discussion in Sec. VI B) and this way entering our extrapolation.

Therefore, Fig. 4 also illustrates the necessity for cross section measurements with the time-of-flight method over a wider energy range from the resonance region up to about 1 MeV, in particular for nuclei involved in the p-process network. Unfortunately, this will be hard to achieve, mostly because isotopically pure samples of the rare p-isotopes are difficult to obtain.

VII. SUMMARY AND OUTLOOK

The (n,γ) cross sections of the p-isotopes ^{102}Pd, ^{120}Te, ^{130,132}Ba, and ^{156}Dy have been measured in a quasi-stellar neutron spectrum corresponding to a thermal energy of kT = 25 keV by means of the activation technique. The results for ^{102}Pd, ^{120}Te, and ^{132}Ba represent the first experimental data, thus replacing rather uncertain theoretical predictions. For ^{130}Ba and ^{156}Dy the previously available experimental information could be significantly extended and improved. The measured cross sections were converted into Maxwellian averaged cross sections for a range of thermal energies between kT = 5 and 100 keV, and further extrapolated to the temperature region of the p-process. The extrapolation still relies on theory and this underscores the necessity for future measurements covering a wider energy range.
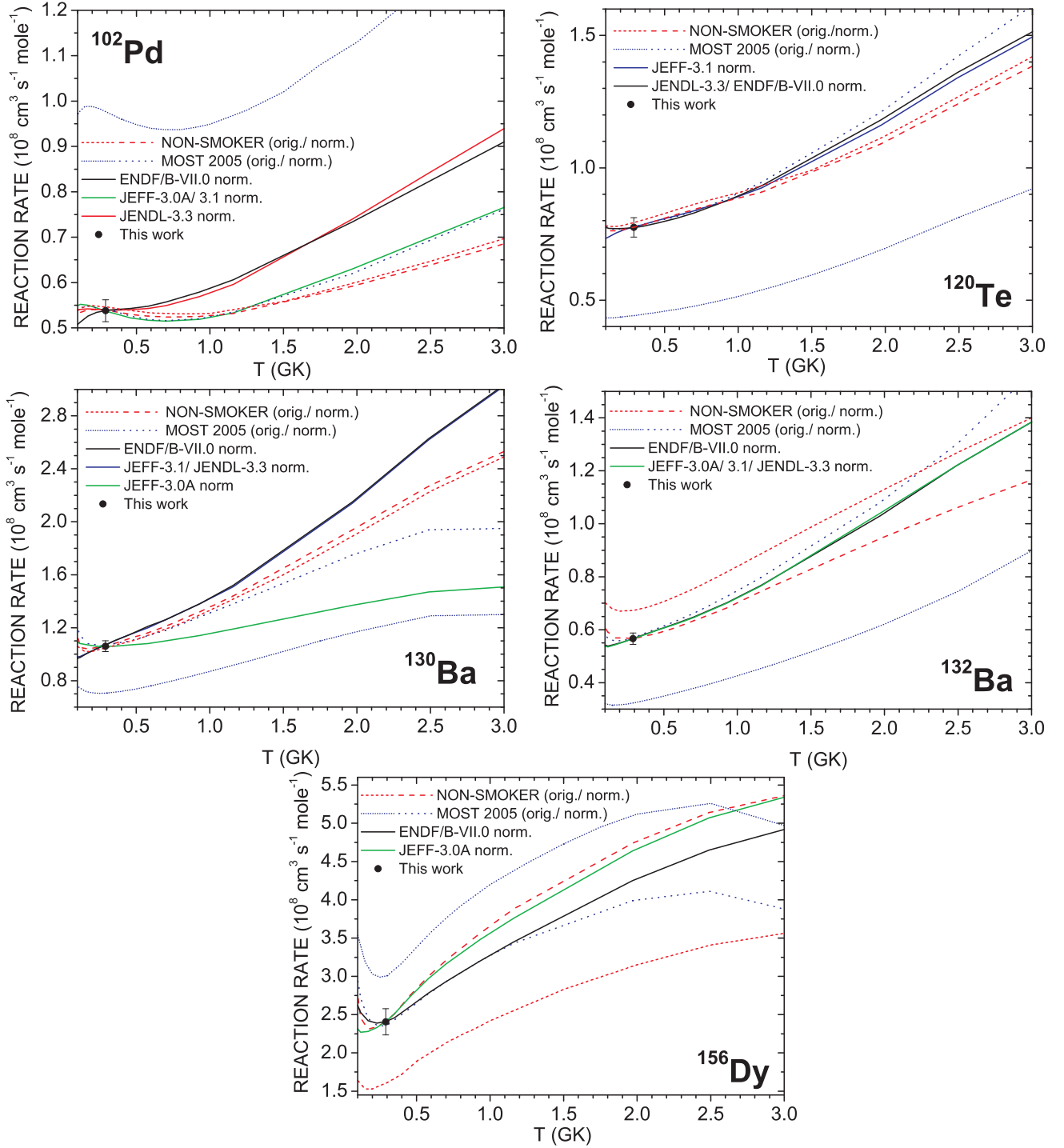
FIG. 4: (Color online) Stellar reaction rates (including f*) for temperatures between T=0.1 and 3 GK. Compared are the temperature-dependences of this work obtained with different extrapolations based on different evaluations. Also shown are the predictions of the Hauser-Feshbach models NON-SMOKER [17, 44] and MOST 2005 [19], each with their original values and renormalized to reproduce our data at kT=25 keV (0.29 GK). It should be noted that above 0.29 GK all values (including the ones from the evaluations) are based on energy dependences derived from Hauser-Feshbach models.

The present work will be complemented by a second paper on the (n,γ) cross sections of ^{168}Yb, ^{180}W, ^{184}Os, ^{190}Pt, and ^{196}Hg, followed by a discussion of the astrophysical implications in a third, concluding paper.

[1] E. Burbidge, G. Burbidge, W. Fowler, and F. Hoyle, Rev. Mod. Phys. **29**, 547 (1957).
[2] K. Langanke and M. Wiescher, Rep. Prog. Phys. **64**, 1657 (2001).
[3] S. Woosley and W. Howard, Astrophys. J. Suppl. **36**, 285 (1978).
[4] S. Woosley and W. Howard, Astrophys. J. **354**, L21 (1990).
[5] M. Rayet, M. Arnould, M. Hashimoto, N. Prantzos, and K. Nomoto, Astron. Astrophys. **298**, 517 (1995).
[6] T. Rauscher, A. Heger, R. Hoffman, and S. Woosley, Astrophys. J. **576**, 323 (2002).
[7] M. Rayet, M. Arnould, and N. Prantzos, Astron. Astrophys. **227**, 271 (1990).
[8] C. Fröhlich, G. Martínez-Pinedo, M. Liebendörfer, F.-K. Thielemann, E. Bravo, W. R. Hix, K. Langanke, and N. T. Zinner, Phys. Rev. Lett. **96**, 142502 (2006).
[9] H. Schatz, A. Aprahamian, J. Görres, M. Wiescher, T. Rauscher, J. Rembges, F.-K. Thielemann, B. Pfeiffer, P. Möller, H. Herndl, et al., Phys. Rep. **294**, 167 (1998).
[10] H. Schatz, A. Aprahamian, V. Barnard, L. Bildsten, A. Cumming, M. Ouellette, T. Rauscher, F.-K. Thielemann, and M. Wiescher, Phys. Rev. Lett. **86**, 3471 (2001).
[11] S. Woosley, D. Hartmann, R. Hoffman, and W. Haxton, Astrophys. J. **356**, 272 (1990).
[12] M. Arnould and S. Goriely, Phys. Rep. **384**, 1 (2003).
[13] I. Dillmann, M. Heil, F. Käppeler, T. Rauscher, and F.-K. Thielemann, Phys. Rev. C **73**, 015803 (2006).
[14] C. Vockenhuber, I. Dillmann, M. Heil, F. Käppeler, N. Winckler, W. Kutschera, A. Wallner, M. Bichler, S. Dababneh, S. Bisterzo, et al., Phys. Rev. C **75**, 015804 (2007).
[15] I. Dillmann, M. Heil, F. Käppeler, R. Plag, T. Rauscher, and F.-K. Thielemann, Proceedings of the 12th Int. Conference on Capture Gamma-Ray Spectroscopy and Related Topcis, Notre Dame/USA, Sept. 4-9, 2005, AIP Conf. Proc **819**, 123 (2005).
[16] W. Hauser and H. Feshbach, Phys. Rev. **87**, 366 (1952).
[17] T. Rauscher and F.-K. Thielemann, At. Data Nucl. Data Tables **75**, 1 (2000).
[18] T. Rauscher and F.-K. Thielemann, At. Data Nucl. Data Tables **79**, 47 (2001).
[19] S. Goriely, Hauser-Feshbach rates for neutron capture reactions (version 08/26/05), http://www-astro.ulb.ac.be/Html/hfr.html (2005).
[20] H. Beer and F. Käppeler, Phys. Rev. C **21**, 534 (1980).

[21] W. Ratynski and F. Käppeler, Phys. Rev. C **37**, 595 (1988).
[22] J. De Laeter, J. Böhlke, P. de Bievre, H. Hidaka, H. Peiser, K. Rosman, and P. Taylor, Pure and Appl. Chem. **75**, 683 (2003).
[23] C. Smith, K. Rosman, and J. De Laeter, Int. J. Mass Spectrom. Ion Phys. **28**, 7 (1978).
[24] J. De Laeter, Astrophys. J. **434**, 695 (1994).
[25] D.-C. Lee and A. Halliday, Int. J. Mass Spectrom. Ion Proc. **146/147**, 35 (1995).
[26] S. Dababneh, N. Patronis, P. Assimakopoulos, J. Görres, M. Heil, F. Käppeler, D. Karamanis, S. O'Brien, and R. Reifarth, Nucl. Instr. and Meth. A **517**, 230 (2004).
[27] D. de Frenne and E. Jacobs, Nucl. Data Sheets **93**, 447 (2001).
[28] T. Tamura, Nucl. Data Sheets **90**, 107 (2000).
[29] Y. Khazov, I. Mitropolsky, and A. Rodionov, Nucl. Data Sheets **1072**, 2715 (2006).
[30] R. Shaheen, Nucl. Data Sheets **75**, 491 (1995).
[31] R. Helmer, Nucl. Data Sheets **103**, 565 (2004).
[32] Z. Chunmei, Nucl. Data Sheets **95**, 59 (2002).
[33] J. Hubbell and S. Seltzer, Table of X-Ray Mass Attenuation Coefficients and Mass Energy-Absorption Coefficients (v. 1.4), National Institute of Standards and Technology, Gaithersburg, MD ; http://physics.nist.gov/PhysRefData/XrayMassCoef/ (2004).
[34] S. Agostinelli, J. Allison, K. Amako, J. Apostolakis, H. Araujo, P. Arce, M. Asai, D. Axen, S. Banerjee, G. Barrand, et al., Nucl. Instr. Meth. A **506**, 250 (2003).
[35] S. Mughabghab, M. Divadeenam, and N. Holden, Neutron Cross Sections, BNL-325, 1st ed., **1** (1981).
[36] S. Mughabghab, Atlas of Neutron Resonances (5th ed.), Elsevier, ISBN 0-444-52035-X (2006).
[37] N. Soppera, M. Bossant, H. Henriksson, P. Nagel, and Y. Rugama, International Conference on Nuclear Data for Science and Technology, Nice/ France 2007, edts. O. Bersillon, F. Gunsing, E. Bauge, R. Jacqmin, S. Leray, EDP Sciences, ISBN: 978-2-7598-0091-9 p. 773 (2008).
[38] K. Shibata, T. Kawano, and T. Nakagawa, Japanese Evaluated Nuclear Data Library Version 3 Revision 3: JENDL 3.3, J. Nucl. Sci. Technol. **39**, 1125 (2002).
[39] M. Chadwick, P. Oblozinsk, M. Herman, N. Greene, R. McKnight, D. Smith, P. Young, R. MacFarlane, G. Hale, S. Frankle, et al., Nuclear Data Sheets **107**, 2931 (2006).
[40] S. Igarasi and T. Fukahori, JAERI 1321 (1991).
[41] T. Bradley, Z. Parsa, M. Stelts, and R. Chrien, *Nuclear*

Cross Sections for Technology, edt. by J.L. Fowler, C.H. Johnson, and C.D. Bowman (National Bureau of Standards, Washington D.C.) p. 344 (1979).

[42] P. Young, V. Arthur, and M. Chadwick, *Proceedings of the IAEA Workshop on Nuclear Reaction Data and Nuclear Reactors: Physics, Design and Safety*, edt. by A. Gandini and G. Reffo, Trieste/Italy, 1996, World Scientific Publishing, Ltd., Singapore p. 227 (1998).

[43] M. Herman, R. Capote, B. Carlson, P. Obložinský, M. Sin, A. Trkov, H. Wienke, and V. Zerkin, Nucl. Data Sheets **108**, 2655 (2007).

[44] T. Rauscher, HTML Interface to NON-SMOKER; Online: http://nucastro.org/nonsmoker (2009).

[45] Z. Bao, H. Beer, F. Käppeler, F. Voss, K. Wisshak, and T. Rauscher, At. Data Nucl. Data Tables **76**, 70 (2000).

[46] B. Allen, J. Gibbons, and R. Macklin, Adv. Nucl. Phys. **4**, 205 (1971).

[47] H. Beer, Technical report KfK-3969, Kernforschungszentrum Karlsruhe p. 14 (1985).

[48] J. Holmes, S. Woosley, W. Fowler, and B. Zimmerman, At. Data Nucl. Data Tables **18**, 305 (1976).

[49] M. Harris, Astrophys. Space Sci. **77**, 357 (1981).

[50] Z. Zhao, D. Zhou, and D. Cai, Nuclear Data for Science and Technology, edts. S. Igarasi (Saikon, Tokyo) p. 513 (1988).